Large-eddy Simulation of a Water Jet Exhausting into Quiescent Air

Valentin Morin, Julien Troyes, François Vuillot, Christophe Bogey

AIAA SciTech Forum
January 3-7, 2022, San Diego, CA & Virtual
AIAA SCITECH 2022 Forum

10.2514/6.2022-2019

Large-eddy simulation of a water jet exhausting into quiescent air

V. Morin* and J. Troyes†
ONERA, University of Toulouse, F-31055 Toulouse, France

F. Vuillot‡
ONERA, University of Paris-Saclay, F-91123, Palaiseau, France

C. Bogey§
Univ Lyon, CNRS, Ecole Centrale de Lyon, INSA Lyon, Univ Claude Bernard Lyon I, Laboratoire de Mécanique des Fluides et d'Acoustique, UMR 5509, 69130 Ecully, France

Large quantities of water are injected in the motor jet plume to reduce the noise levels generated by rocket engines. This study focuses on the water injection system and more precisely on the destabilization of the liquid jet that leads to a spray system. For that purpose, a large-eddy simulation (LES) is conducted for an experimental water jet of the literature. It is a sprinkler whose Reynolds number is $Re = 82,000$ and nozzle exit diameter is $D = 4.37$ mm, corresponding to injectors used for jet noise reduction studies at a reduced scale. A diffuse interface method is used to calculate the dense liquid phase, and the dispersed phase containing droplets is calculated with an Eulerian solver. Transfers between the dense and the dispersed phases are modeled in the coupling procedure, including the atomization process. A synthetic-eddy method (SEM) is also applied in the water inlet region to force the jet transition. Different grid sizes are tested to evaluate the sensitivity of the results. The evolution of the mean jet radius along the axis is found to be in good agreement with the experimental data and the most unstable frequency obtained in the jet shear layer by the LES is similar to that observed in the experiment. Finally, a methodology based on the instability waves developing at the interface is used to estimate the diameter of atomized droplets. First qualitative results of the simulation with atomization are presented.

I. Introduction

For a space launcher, the noise [1] generated by the jet engines induces unsteady stresses on the rocket, its payload, and the launch pad. When the jet is supersonic, several noise components are emitted. They include turbulent mixing noise [2], as for subsonic jets, but also Mach waves generated by supersonic convective structures [3], broadband-shock-associated-noise [4, 5] and possibly screech noise [6] coming from shock and turbulence interactions. Research has been made for many years to reduce the acoustic levels or at least to lower their damaging effects. In particular, injecting large quantities of water in the motor jet plume was found to effectively decrease the jet noise levels [7–9]. The hot and fast exhaust gas transfers momentum and heat fluxes to the droplets of the spray formed by water injection devices, leading to acoustic power loss. However, the interaction mechanisms between droplets and turbulent structures in the mixing layer of a gas jet remain not well understood. To better understand these mechanisms, the droplet characteristics such as their size, velocity and mass fraction have to be identified. When water exhausts from a nozzle, the transition between the dense phase regime where the liquid and gas are clearly separated and the dispersed phase containing droplets is called atomization. This phenomenon consists of multiple processes. In the first one, the shear at the liquid-gas interface generates Kelvin-Helmholtz (KH) instabilities [10–13] which are amplified due to the presence of a density gradient, a velocity gradient and a surface tension. Then, for axisymmetric jets, azimuthal Rayleigh-Taylor (RT) instabilities emerge and trigger the breakup of the dense liquid phase into large ligaments [14, 15]. This process is referred as primary atomization. The ligaments break up into multiple droplets, which can themselves be fragmented into smaller

*PhD student, Multi-physics for Energetics Department, valentin.morin@onera.fr
†Research scientist, Multi-physics for Energetics Department, julien.troyes@onera.fr
‡Research scientist, Multi-physics for Energetics Department, françois.vuillot@onera.fr
§Research scientist, christophe.bogey@ec-lyon.fr, AIAA Associate Fellow

droplets. This last process is referred as secondary atomization. If the primary liquid breakup and the evolution of large liquid ligaments can be accurately solved by direct numerical simulation (DNS) [16, 17] or large-eddy simulation (LES) [18, 19], the secondary breakup and the generation of small droplets must be modeled.

The influence of parameters such as the injection angle, the distance to the nozzle exit and the liquid mass flow rate of the water jets on noise reduction has been studied in several experimental works [7–9, 20]. Simulations have also been performed [21–23] and focus on the modeling of the interactions between the water and the motor jet plume. The studies of Fukuda et al. [21] and Capecelatro and Buchta [22] considered the interactions between the droplets and the gas jet, and did not take into account the interactions between the water dense phase and the gas. In Fukuda et al. [21], the noise suppression using Reynolds-Averaged-Navier-Stokes (RANS) simulation was in good agreement with experimental data, but the droplet size was arbitrarily fixed. Thus, the influence of the injector geometry and the exit velocity on the droplet diameter cannot be investigated. Furthermore, RANS simulation cannot account for the interactions of the droplets with the turbulent structures in the gas jet mixing layer. Capecelatro and Buchta [22] implemented a DNS of a jet noise reduction with droplets, and obtained a good agreement with experimental results. Their calculation enabled to analyze the droplet behavior in the turbulent mixing layer, but cannot be conducted for a complex configuration with multiple water injectors. On the other hand, Salehian et al. [23] performed a high-fidelity simulation of the interactions between a water dense phase and a gas. They directly calculated the atomization of the largest droplets and ligaments using a volume-of-fluid method, but did not resolve the small droplets. In their simulation, if noise reductions appeared well predicted for low acoustic frequencies, noise suppression was overestimated for higher frequencies. The droplets were too large due to the surface tension neglected in the model. The present work aims to use a hybrid method to calculate both the dense phase of the jet including surface tension effects and the simulation of the small droplets in the spray. In that way, the largest droplets can be calculated by the dense phase solver as in Salehian et al. [23], and the smallest droplets atomized after the breakup of ligaments, are taken into account. The exchange area between the two phases, as well as the momentum, heat and mass transfers and consequently the noise reduction are thus expected to be accurately calculated. The present approach, by considering in the same simulation both the dense and dispersed liquid phases, will complement the previous computational works mentioned above.

To investigate jet noise reduction with water injection, simulations will be conducted on the MARTEL bench configuration [24]. The objective of the present work is to validate the numerical methodology for the water injection. For that, calculations are carried out on an experimental sprinkler case [25, 26] whose parameters correspond to those of the water injectors used for jet noise reduction experiments at the MARTEL bench [7, 20]. The paper focuses on the simulation of the primary atomization process and the ligament breakup of the water injector. At this point, fragmentation and coalescence of droplets, and droplet re-absorption into the dense phase are not taken into account. Two solvers from the CEDRE code developed at ONERA [27] are used for the simulation. The first one is a Navier-Stokes solver for the dense phase, using a diffuse interface method. The evolution of the liquid mass fraction is calculated and the interface position can only be estimated from post-processing results. It differs from front-tracking [28, 29] or front-capturing [17, 30] methods where the interface geometry is modeled. These latter techniques are more accurate but also more difficult to implement in complex configurations and can suffer from mass non-conservation [31]. Therefore, it has been chosen to use the diffuse interface method whose efficiency was proven in the CEDRE code for atomization concerns [32, 33]. A synthetic-eddy method (SEM) proposed by Jarrin et al. [34, 35] and Jarrin [36] is also applied to seed the interface instabilities of the dense phase regime. The second solver is an Eulerian resolution of the dispersed phase based on the Williams-Boltzmann kinetic equations. Mass, momentum and energy transfers between the dense and dispersed phase solvers are modeled to take into account the ligament breakups and the drag force on the droplets.

The present paper is organized as follows. The experimental setup is first presented in section II. Then, the numerical procedures, namely the dense and the dispersed phase solver and the SEM, are described in section III. In section IV, a preliminary study about the setup of the SEM is shown. Then the instability of the jet with the simulation of the dense phase only is investigated. Finally, results including the dispersed phase resolution are shown.

II. Experimental configuration

A. Experimental setup

The configuration investigated is based on the water jet in the experiments of Stevenin [25] and Stevenin et al. [26]. The injector, depicted in figure 1, is the sprinkler RB46 designed for crop irrigation. It is composed of an elbow, a long slightly converging section with an angle of 1° containing four perpendicular stabilizing fins, followed by a 34° converging section and ended by a small cylindrical nozzle with an exit diameter $D = 4.37$ mm.

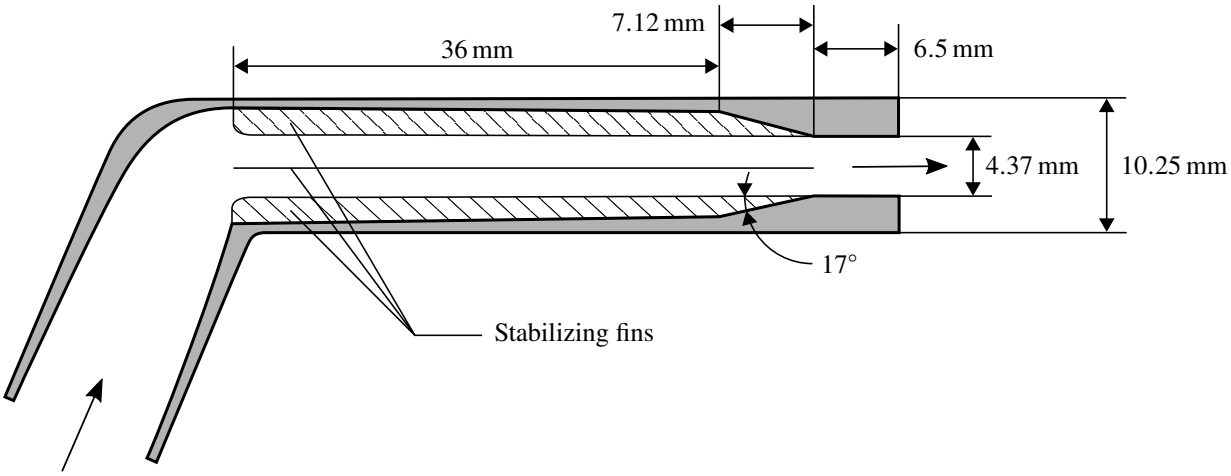

Fig. 1 Experimental water nozzle.

The main characteristics of the regime of interest are given in table 1. Four non-dimensional numbers are defined to describe the jet. They indicate which phenomena have preponderant effects on the flow. The variable U_l is the nozzle exit velocity, U_g is the gas velocity, ρ_g and ρ_l are the gas and liquid densities, ν_l and μ_l are the kinematic and dynamic viscosities of the liquid and γ is the surface tension coefficient. The liquid Reynolds number Re_l is the ratio between the fluid inertia forces and the liquid molecular viscosity. It is equal to 82,000, revealing that molecular viscosity is negligible with respect to the inertia forces and that the jet is in a turbulent regime. The Weber number We compares the inertia forces with capillarity. Two definitions, We_l and We_g, are given in table 1 depending whether the number is relative to the liquid or to the gas phase. The Ohnesorge number Oh is the ratio between molecular viscosity and capillarity.

Table 1 Injector's parameters

	$U_l\ (m/s)$	Re_l	We_g	We_l	Oh
Definition	-	$\frac{U_l D}{\nu_l}$	$\frac{\rho_g (U_l - U_g)^2 D}{\gamma}$	$\frac{\rho_l (U_l - U_g)^2 D}{\gamma}$	$\frac{\mu_l}{\sqrt{\rho_l \gamma D}}$
Value	24.37	82,000	43	36,000	0.0023

Each non-dimensional number taken individually does not give relevant information on the atomization regime but their combination does. For that, experimental diagrams based on the non-dimensional numbers have been proposed by authors such as Reitz [37], Lasheras and Hopfingers' [38] and Stahl's et al. [39]. The liquid breakup regime of the present configuration stands between the "wind induced" and "atomization" regimes in these diagrams, indicating that the liquid breakup occurs a few diameters downstream of the nozzle exit and the size of the droplets are smaller than the jet diameter.

B. Mesh and boundary conditions

The mesh and the assumptions made for the numerical model are presented in this section. Choice has been made to simulate the fluid only in the last cylindrical section of the injector. Therefore, the elbow, the converging section and the stabilizing fins are not taken into account. The injector is considered cylindrical and his length is $3.12D$. The numerical domain is a large cylinder box, whose transverse cut is presented in figure 2(a).

The boundary conditions are summarized in table 2, where U, T and p are respectively the velocity, the static temperature and the static pressure. A smooth co-flow of a velocity of $2\,\mathrm{m\,s^{-1}}$ is applied at the air inlet boundary in order to increase the robustness of the simulation. This leads to a small reduction of the relative velocity between the liquid and gas and hence of the Weber number. The outlet is defined differently whether the fluid enters or exits the domain. When the fluid exits the domain, only pressure is imposed at the boundary. However, when the direction of the flow is oriented toward the domain, the velocity, the temperature and the direction of the fluid, specified by the user, are

imposed at the boundary cells. For each limit, other than prescribed variables are calculated to ensure continuity.

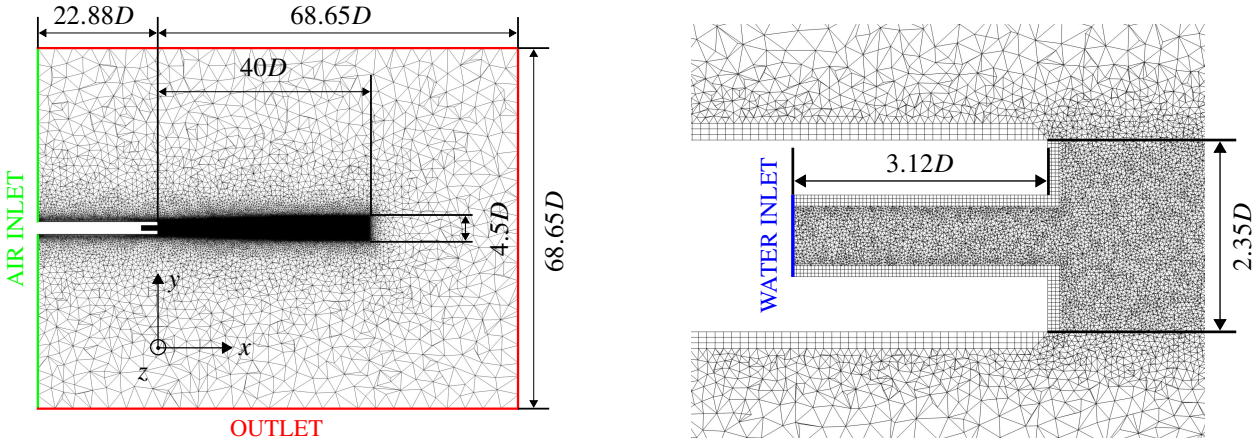

Fig. 2 Mesh representation : (a) full mesh, (b) zoom.

Table 2 Boundary conditions

	prescribed variables	species	U[m s^{-1}]	p[kPa]	T[K]
air inlet	U, T	air	2	-	294.15
water inlet	U, T	water	24.37	-	294.15
outlet in	U, T	air	2	-	294.15
outlet out	p	-	-	99.97	-

Simulations have been carried out on the mesh presented in figure 2(a), which refined area is forty diameters long, and for two specific grid sizes $\delta_{grid} = 0.0229D$ and $\delta_{grid} = 0.0183D$, where $\delta_{grid} = 6 \times V_{cell}/A_{cell}$ is the equivalent cell diameter with V_{cell} and A_{cell}, respectively, the volume and the area of a cell, to evaluate the influence of the mesh resolution on the results. The finer mesh contains 28.2 million cells and the coarser one 15.4 million cells.

III. Numerical procedure

A. Dense phase solver

The dense phase flow solver used is the CHARME solver from the CEDRE code developed at ONERA. It is based on a four-equations formulation. This is a model where the fluid is considered locally homogeneous regarding velocity, pressure, and temperature. A more accurate model could take into account velocity, pressure and temperature discontinuities between liquid and gas phases but it would be more complex to implement and is not retained in this work. The present model is a mono-fluid approach where liquid and gas mass fractions, and hence mean density, are calculated. Each cell is a mixture of the two phases and the liquid-gas interface is diffused in the mesh. Its position can be estimated from post-processing results using special criteria.

The vector of conservative variables is expressed by $\vec{Q} = \left(\rho Y_l, \rho Y_g, \rho \vec{U}, \rho e_t\right)^t$. The four governing equations, namely the liquid and gas mass, the momentum and the energy conservations, can be written as :

$$\frac{\partial \vec{Q}}{\partial t} + \vec{\nabla} \cdot \vec{F}_C = \vec{\nabla} \cdot \vec{F}_D - \vec{S} \tag{1}$$

where $\vec{S}$ denotes the exchange term between the dense phase solver and the dispersed phase solver and will be described later in section III.B. The vectors $\vec{F}_C$ and $\vec{F}_D$ are, respectively, the convective and dissipative fluxes given by :

$$\vec{F}_C = \vec{Q} \otimes \vec{U} + p \begin{pmatrix} 0 \\ 0 \\ \bar{\bar{I}} \\ \vec{U} \end{pmatrix} \tag{2}$$

and

$$\vec{F}_D = \begin{pmatrix} -\vec{J}_l \\ -\vec{J}_g \\ \left(\bar{\bar{\tau}} - \bar{\bar{\tau}}_c\right) \\ \left(\bar{\bar{\tau}} - \bar{\bar{\tau}}_c\right) \cdot \vec{U} - \vec{J}_e \end{pmatrix} \tag{3}$$

The capillary stress tensor $\bar{\bar{\tau}}_c$ is expressed by :

$$\bar{\bar{\tau}}_c = \gamma \parallel \vec{\nabla}\alpha_l \parallel \left(\bar{\bar{I}} - \frac{\vec{\nabla}\alpha_l}{\parallel \vec{\nabla}\alpha_l \parallel} \otimes \frac{\vec{\nabla}\alpha_l}{\parallel \vec{\nabla}\alpha_l \parallel}\right) \tag{4}$$

with

$$\alpha_l = \frac{\rho Y_l}{\rho_l} \tag{5}$$

The fluxes $\vec{J}_l$ and $\vec{J}_g$ are formulated by the Fick's law :

$$\vec{J}_l = -\rho D_l \vec{\nabla} Y_l \tag{6}$$

$$\vec{J}_g = -\rho D_g \vec{\nabla} Y_g \tag{7}$$

Assuming that the heat flux is driven by the Fourier's law, $\vec{J}_e$ is given by :

$$\vec{J}_e = -\lambda \vec{\nabla} T + h_l \vec{J}_l + h_g \vec{J}_g \tag{8}$$

where h_l and h_g are, respectively, the specific enthalpies of liquid and gas and λ is the thermal conductivity.

A thermodynamic closure is necessary to link density, pressure and temperature. Density is directly deduced from the conservative variables $\rho = \rho Y_l + \rho Y_g$. Introducing volume fractions α_l and α_g, and densities of pure phases ρ_l and ρ_g, density reads $\rho = \alpha_l \rho_l + \alpha_g \rho_g$. A compressible liquid equation of state is used to link ρ_l to pressure and temperature as $\rho_l = \rho_0 \left[1 + \beta_0 (p - p_0)\right] / \left[1 + \alpha_0 (T - T_0)\right]$, β_0 being the isothermal compressibility of liquid and α_0 the isobaric dilatation coefficient, where subscript 0 refers to the reference state. An ideal gas assumption is used for thermodynamic closure of the gas phase, yielding $\rho_g = p/rT$. A mixture law, whose details can be found in Le Touze [40], links the previous equations of state to find the mean pressure and temperature of the mixture when both liquid and gas are present in a cell. The governing equations are filtered by the grid at the length scale $\Delta = \delta_{grid}$. The filtered variables, denoted by a tilde, are calculated by the solver and the effects of the eddies smaller than Δ are modeled by a wall-attenuated Smagorinsky scheme under Boussinesq assumption where turbulent viscosity is given by $\mu_t = \bar{\rho} min \left(C_s \Delta, \kappa l_w\right)^2 \sqrt{2 I_D}$ [41], where l_w is the distance from the nearest wall, $\kappa = 0.41$ is the Von Kàrmàn constant, C_s is set to 0.1, and I_D is given by :

$$I_D = \sum_{ij} D_{ij} D_{ij} \tag{9}$$

with

$$D_{ij} = \frac{1}{2}\left(\frac{\partial \tilde{U}_i}{\partial x_j} + \frac{\partial \tilde{U}_j}{\partial x_i}\right) \tag{10}$$

The numerical discretization relies on a finite volume method on a 3D unstructured mesh. A Runge-Kutta second-order implicit scheme is used for temporal integration. A time step $\Delta t = 0.1$ µs is set for all simulations, yielding a maximum Courant–Friedrichs–Lewy number $CFL_{max} = max\left(\|\vec{U}\| + c\right) \Delta_t / min\left(\delta_{grid}\right)$, where c is the speed of

sound, below 1.8. The diffusive fluxes are calculated using a second-order cell-centered scheme. The convective fluxes are calculated using the Harten Lax Van Leer contact wave "HLLC" method based on the resolution of a Riemann problem [42]. A low Mach number version is used, which reduces numerical dissipation for incompressible flows. Cell-centered variables are interpolated to faces using a multi-slope method [40, 43]. Unlike mono-slope techniques classically used in finite-volume method, a scalar weighting of slopes, calculated at the different faces of a cell, is used to estimate the interpolated variables to each face, which reduces the numerical diffusion.

B. Dispersed phase solver

The dispersed phase solver is the SPIREE solver from the CEDRE code. It is based on an Eulerian calculation of droplets. The probability density function of droplet number n is calculated using the Williams-Boltzmann kinetic equation method [44]. The velocity and temperature are assumed to be equal for every droplet in a cell. The vector of conservative variables is $\vec{Q}_d = \left(n, \alpha_d\rho_d, \alpha_d\rho_d\vec{U}_d, \alpha\rho_d e_{d_t}\right)^t$, where α_d is the droplets volume fraction, ρ_d is their density, $\vec{U}_d$ is their velocity, and e_{d_t} is the total energy of the dispersed phase. The governing system for the dispersed phase can be written as :

$$\frac{\partial\vec{Q}_d}{\partial t} + \vec{\nabla}\cdot\vec{F}_{d_C} = \vec{S} \tag{11}$$

where $\vec{F}_{d_C} = \vec{Q}_d \otimes \vec{U}_d$ is the convective flux vector. Every droplet are assumed to have the same diameter D_d.

The source term $\vec{S}$ introduced in equation (1) and (11) accounts for the mass, momentum and energy transfers between the dense and dispersed phase solvers due to atomization, and for the momentum transfer due to the drag force on a droplet. It is expressed by :

$$\vec{S} = \begin{pmatrix} S_a \\ 0 \\ n\vec{F}_d + S_a\vec{U} \\ S_a\left(c_p(T_a) + \frac{1}{2}\vec{U}^2\right) + n\vec{F}_d\cdot\vec{U}_d \end{pmatrix} \tag{12}$$

where S_a is the mass transfer per unit of volume and time due to atomization, $\vec{F}_d$ is the drag force of the fluid to the particles and c_p is the heat capacity of droplets at constant pressure. The mass transfer S_a is expressed by $S_a = \rho Y_l f_a \lambda_a(Y_l)$, where f_a is a specific frequency for the atomization process and λ_a is a function depending on the liquid mass fraction. The frequency f_a accounts for the rate of the atomization process. In this study, f_a is the turbulent frequency $f_a = \sqrt{2I_D}$. It ensures that the mass atomization rate is all the more important as the flow is turbulent. The function λ_a enables atomization only when the liquid mass fraction of the dense phase is negligible. This means that droplets cannot be formed inside a ligament, but only at the liquid-gas interface. The function λ_a is given by $\lambda_a = 1 - \tanh\left(4Y_l^2\right)$. During atomization, the ejected particles velocity $\vec{U}_d$ is the local velocity of the fluid U.

The drag force exerted by the flow on a droplet F_d can be expressed by :

$$F_d = \frac{\pi D^2}{4}\rho C_d \parallel \vec{U} - \vec{U}_d \parallel^2 \tag{13}$$

where C_d is the drag coefficient of the particle. It has different formulations depending on the droplet Reynolds number defined as $Re_d = \rho_d D_d \parallel \vec{U} - \vec{U}_d \parallel / \mu_g$, where μ_g is the gas dynamic viscosity and ρ_d is the droplet density. According to the correlation of Schiller and Nauman [45], the corresponding drag coefficient is :

$$C_d = \begin{cases} \frac{24}{Re_d} & \text{if } Re_d < 1 \\ \frac{24}{Re_d}\left(1 + 0.15Re_d^{0.687}\right) & \text{if } 1 \leq Re_d \leq 1000 \\ 0.445 & \text{if } 1000 < Re_d \end{cases} \tag{14}$$

The source term $\vec{S}$ enables mass, momentum and energy transfers between the two solvers. The time steps used for the solvers are identical allowing $\vec{S}$ to be calculated at each iteration.

C. Synthetic-eddy method (SEM)

The SEM proposed by Jarrin et al. [34] and Jarrin [36] is used in this work to obtain a disturbed flow state at the nozzle exit. It consists in injecting coherent structures through the water inlet boundary condition. An independent algorithm is used to generate random eddies in a small box surrounding the inlet boundary and to calculate their position over time. A fluctuating velocity signal is then imposed at the water inlet boundary cells depending on the positions of the eddies.

1. Eddy generation

The principle of the SEM algorithm is depicted in figure 3. A box is defined as an extrusion of the inlet surface. It is located between $x = -\sigma$ and $x = +\sigma$, where $x = 0$ is the axial position of the inlet, and σ is the size of a turbulent spot. A number of N structures are introduced randomly in the box and are convected at a mean velocity U_{inj} specified by the user, according to Taylor's frozen turbulence hypothesis. When an eddy comes out of the box, it is randomly re-injected at the box inlet. Under such conditions, random eddies are permanently crossing the inlet boundary.

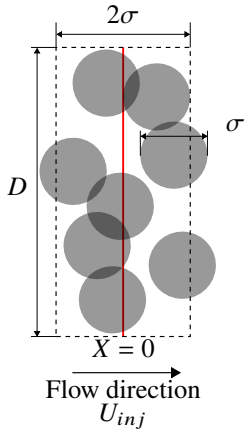

Fig. 3 Principle of eddy generation with SEM.

2. Turbulent signal

Once eddies are generated and convected in the SEM box, they must be linked to the dense phase solver. The following fluctuating velocity signal is prescribed at a point on the water inlet surface $\vec{X} = (0, y, z)$ for each coordinate $i = (x, y, z)$:

$$u_i^{"}(\vec{X}, t) = \frac{1}{\sqrt{N}} \sum_{k=1}^{N} \epsilon_{ik} f_\sigma \left(\vec{X} - \vec{X}_k(t) \right) \tag{15}$$

where k is the index of a spot, $\vec{X}_k = (x_k, y_k, z_k)$ is the center of the spot k and ϵ_{ik} is randomly equal to -1 or 1. The total velocity at the inlet is given by :

$$U_i(\vec{X}, t) = U_{inj} + \sum_{j=1}^{3} A_{ij} u_j^{"} \tag{16}$$

where the tensor $\bar{\bar{A}}$ depends on the Reynolds tensor $\bar{\bar{R}}$ and is given by :

$$\bar{\bar{A}} = \begin{pmatrix} \sqrt{R_{11}} & 0 & 0 \\ \frac{R_{21}}{A_{11}} & \sqrt{R_{22} - A_{21}^2} & 0 \\ \frac{R_{31}}{A_{11}} & \frac{R_{32} - A_{21} A_{31}}{A_{22}} & \sqrt{R_{33} - A_{32}^2} \end{pmatrix} \tag{17}$$

The function f_σ accounts for the influence of each eddy on the velocity depending on the distance between the center of the spot $\vec{X}_k(t)$ and the point $\vec{X}$.

$$f_\sigma\left(\vec{X}-\vec{X}_k(t)\right)=\frac{\sqrt{V_{box}}}{\sigma^3}f\left(\frac{x-x_k(t)}{\sigma}\right)f\left(\frac{y-y_k(t)}{\sigma}\right)f\left(\frac{z-z_k(t)}{\sigma}\right) \tag{18}$$

In this case, f is the tent function :

$$f(x)=\begin{cases}\sqrt{\frac{3}{2}}(1-|x|) & \text{if } |x|<1\\ 0 & \text{otherwise}\end{cases} \tag{19}$$

The spots are convected at the mean velocity U_{inj} in the direction x. Thus, the evolution of the center of a spot k is determined by :

$$\vec{X}_k(t+dt)=\vec{X}_k(t)+dt\vec{U}_{inj} \tag{20}$$

IV. Results and discussions

A. SEM preliminary results

A preliminary parametric analysis evaluating different parameters of the SEM has been conducted with a focus on the injector exit conditions. To reduce simulation cost, these runs have been conducted on meshes with a limited refined area in X direction, up to $X/D = 5$, presented in figure 4.

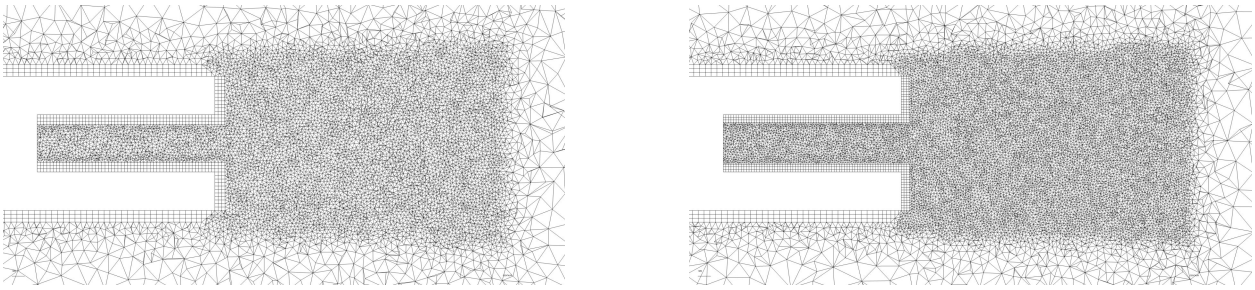

(a) **(b)**

Fig. 4 Reduced meshes cuts : (a) $\delta_{grid} = 0.0229D$, (b) $\delta_{grid} = 0.0183D$.

The size of the spots has been arbitrarily set to $\sigma = D/10$. The number of spots in the box has been set to $N = 100$, corresponding to the ratio between the inlet area $A_{inlet} = \pi D^2/4$ and the spot projected area $A_{spot} = \pi\sigma^2/4$, to ensure that the inlet boundary is always filled with spots. A field of the liquid Q criterion defined as $Q_l = \alpha_l^5 Q$ obtained for the grid spacing $\delta_{grid} = 0.0183D$ is represented in figure 5. SEM spots can be seen inside the injector downstream of the water inlet, marked by maxima of Q_l.

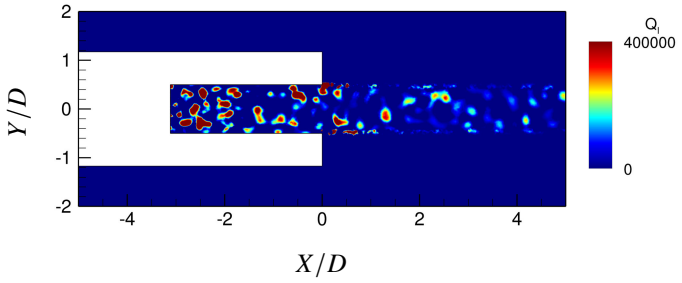

Fig. 5 Q_l criterion field in (X, Y) plane at $t = 111.5\ D/U_l$.

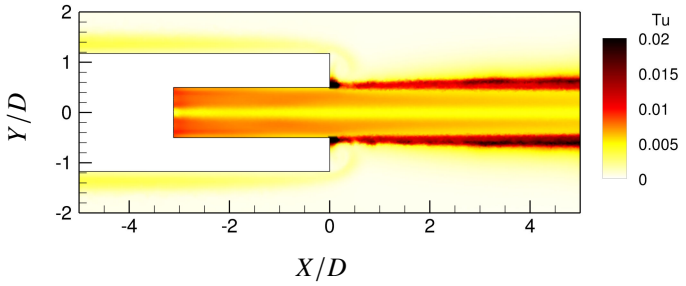

Fig. 6 Mean turbulent intensity field in (X, Y) plane.

The turbulence intensity $Tu = (2TKE/3)^{1/2}/U_{ej}$, where $TKE = \left(\langle u_x^{"2}\rangle + \langle u_y^{"2}\rangle + \langle u_z^{"2}\rangle\right)/2$, is shown in figure 6. It is approximately equal to 1 % near the water inlet and decreases farther downstream, indicating that turbulence is dissipated in the liquid core with the axial distance. The levels around the axis are almost half the value of the levels at $Y/D > 0.1$ in the injector, that may be due to the axisymmetric inlet condition implementation. As the development of waves at the liquid-gas interface is triggered by small perturbations around $r/D = 0.5$, the low turbulent intensity level observed at the center of the jet should not have effect on the jet transition and is no further investigated.

The power spectral density of U_x is plotted in figure 7(a) for different grid sizes at $r/D = 0.4$ and $X/D = 0$, and in figure 7(b) for different axial positions at $r/D = 0.5$ with the grid size $\delta_{grid}/D = 0.0183$. The signals are recorded during 35 ms = 195.2 D/U_l. For each one, the power spectral density is calculated using a Welch method dividing the signal in 10 temporal windows with a 50 % overlap. For a given radial position, the spectra are recorded in four azimuthal planes then averaged. For the coarser mesh in figure 7(a), the cut-off frequency related to the grid size is observed around $St \simeq 1$, whereas it is higher and close to $St = 2.5$ for the finer mesh. This cut-off frequency corresponds to a wave discretized over 720 time steps and over 22 cells for the finer mesh, assuming a phase velocity of 24.37 m s^{-1}. As seen in figure 7(b), a broadband spectrum is generated at the inlet condition at $X/D = -3.12D$, decreasing for $St \geq 3$. The spectra at $X/D = -1.56$ and $X/D = 0$ decrease sooner than the spectrum at $X/D = -3.12$, suggesting that the mesh cuts off the frequencies higher than $St \geq 2.5$. The spectra at $X/D = -1.56$ and $X/D = 0$ are similar, indicating that the grid size has no longer effect at $r/D = 0.4$, for $X/D \geq -1.56$.

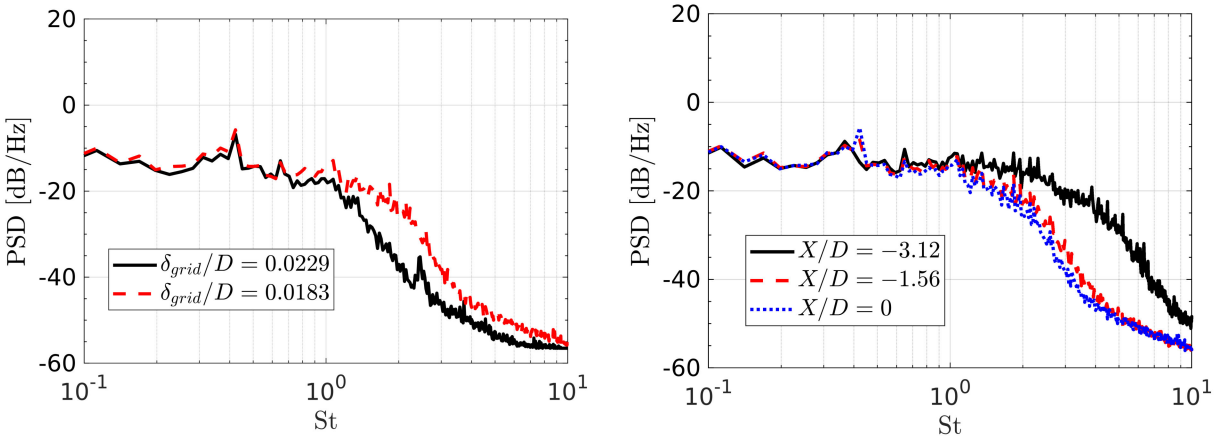

(a) **(b)**

Fig. 7 Power spectral density of U_x obtained at $r/D = 0.4$ using SEM with $N = 100$ and $\sigma/D = 10$: (a) for $\delta_{grid}/D = 0.0183$, (b) at $X = 0$ for $\delta_{grid}/D = 0.0229$ and $\delta_{grid}/D = 0.0183$.

These preliminary results show that a turbulent inflow condition is reproduced by the SEM for parameters $N = 100$ and $\sigma = D/10$. A broadband signal is obtained at $X = 0$ and $r/D = 0.4$, which should allow the jet transition. Therefore, the SEM parameters above will be used for the simulation of the real jet. It should be noted that the goal is to excite the velocity signal over a large frequency range so that the instability waves at the liquid-gas interface have sufficient energy

to develop. Further details on the effect of the turbulent profile in the nozzle on the atomization are not studied in this paper but can be found in the works of Wu et al. [46] and Stahl et al. [39].

B. Analysis of the dense phase instabilities

1. Jet transition

The simulation of the jet has been conducted using the finer mesh with the grid size $\delta_{grid}/D = 0.0183$ refined down to $40D$ from the nozzle exit, as illustrated in figure 2(a), with and without SEM. The instantaneous isosurface $\alpha_l = 0.15$ at $t = 20\,\text{ms} = 111.5\ D/U_l$ and streamlines are represented in figure 8. Without SEM, in figure 8(a), the liquid jet remains laminar between $X = 0$ and $X/D = 40$. With SEM, in figure 8(b), the liquid jet becomes unstable at $X/D \simeq 15$ where small oscillations appear at the interface. These oscillations are amplified as the distance from the nozzle increases. Therefore, the SEM has significant effects on the interface destabilization, and is essential for the jet transition.

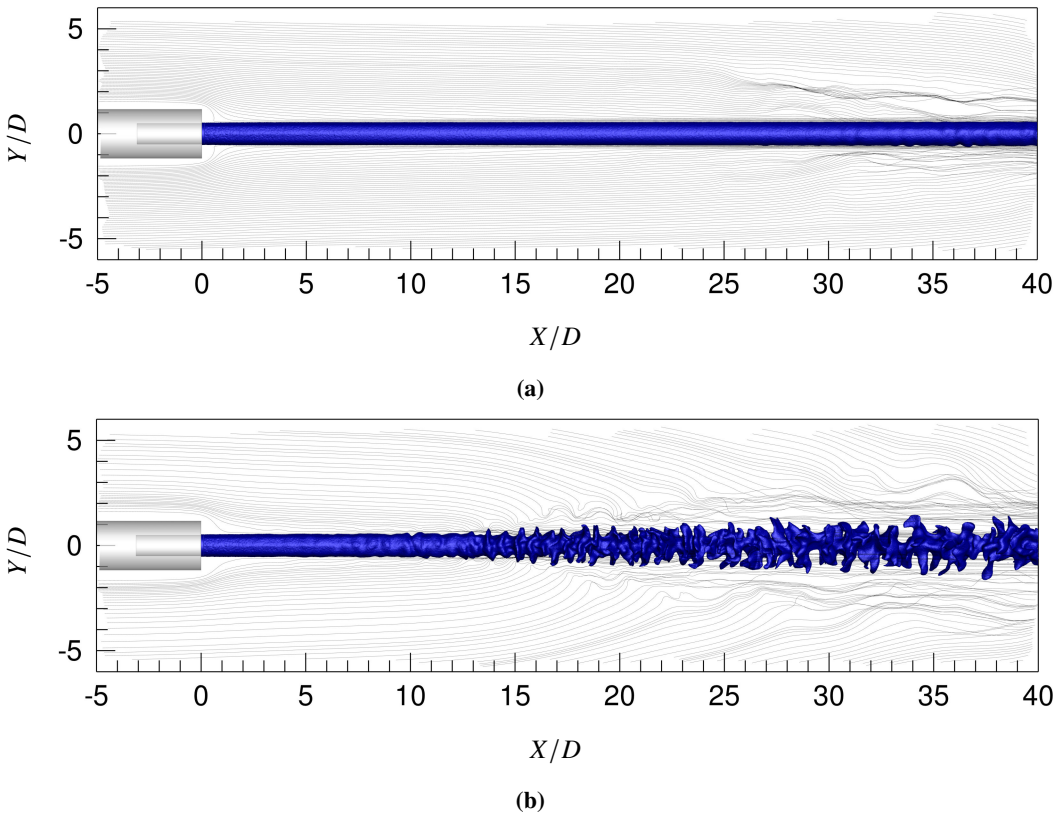

Fig. 8 Instantaneous isosurface of volume fraction $\alpha_l = 0.15$ and streamlines at $t = 111.5\ D/U_l$: (a) without SEM, (b) with SEM ($N = 100$, $\sigma/D = 10$).

The instantaneous isosurface of Q criterion $Q = 10^8$ is displayed in figure 9. The eddy structures are mostly concentrated at $X/D \simeq 20$ and $r/D \simeq 1$. The instantaneous isosurface of variable $Q_l = \alpha_l^5 Q$ is shown in figure 10 to highlight the eddies inside the liquid core. These structures are less visible as the distance from the nozzle exit increases.

The turbulent intensity field obtained in the (X, Y) plane is represented in figure 11. The maximum levels reach 25 % and are located between $X/D = 15$ and $X/D = 20$. It can be pointed out that there is a significant difference in the turbulence intensity field in the mixing layer between $X/D < 15$ and $X/D > 20$. The interface instabilities seen in figure 8(b) develop in the laminar part of the jet before $X/D = 15$ and their amplification lead to a jet transition for $X/D > 20$ to a turbulent regime. To confirm that the jet transition is well reproduced by the simulation, comparisons with the experimental data are presented in the next section.

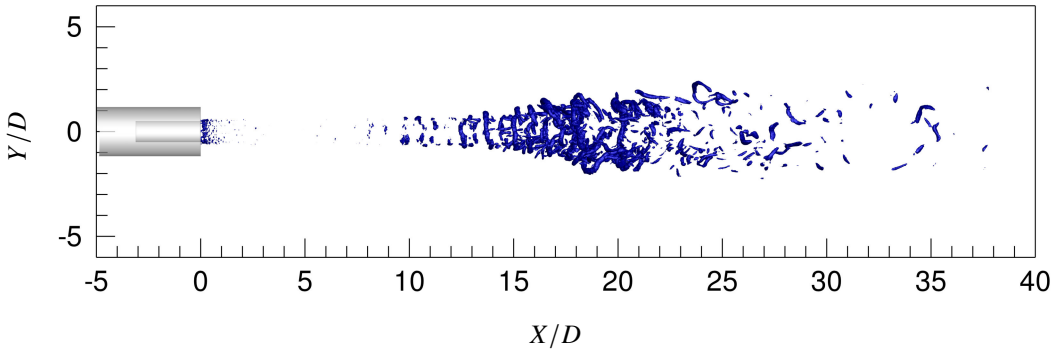

Fig. 9 Isosurface of $Q = 10^8$ at $t = 111.5\ D/U_l$.

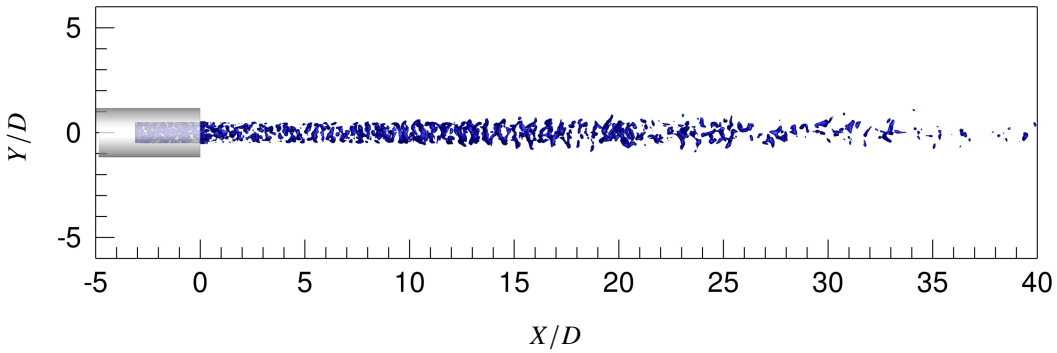

Fig. 10 Isosurface of $Q_l = 10^5$ at $t = 111.5\ D/U_l$.

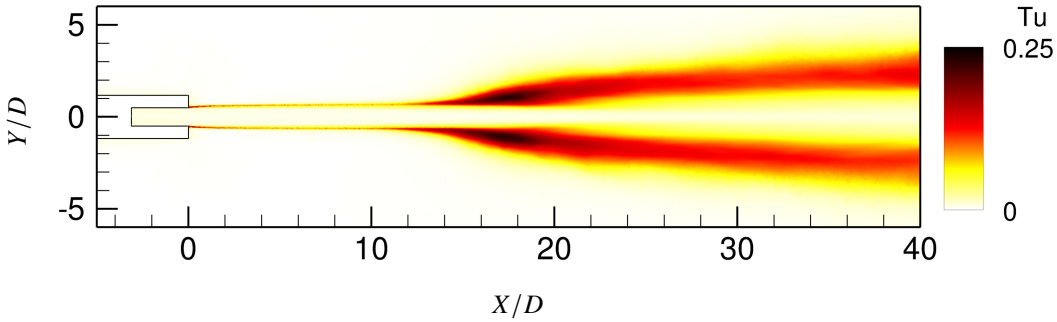

Fig. 11 Mean turbulent intensity field in (X, Y) plane.

2. Liquid-gas interface position : comparison with experiments

The mean liquid-gas interface position is quite difficult to measure because it relies on an arbitrary criterion. Experimentally [25], a shadowgraphy technique is used for its measurement, by locating the liquid-gas interface on a series of pictures recorded by a high-speed camera. The method is schematized in figure 12.

On each recorded camera shot perpendicular to the jet axis in the experiments, the top and the bottom interfaces, referred to as interfaces 1 and 2 in figure 12, have been identified using an image processing. The radius $R(X)$ is the distance of the interface from the center axis at the abscissa X. A number of 500 pictures have been processed, yielding 1,000 data sets of $R(X)$ for the measurement of the mean radius $R(X)$.

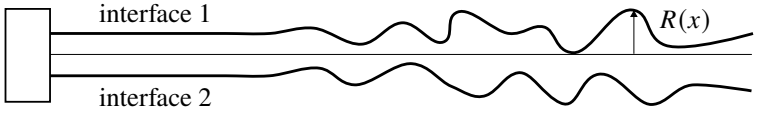

Fig. 12 Interface detection method.

In a laminar case, a few diameters downstream of the nozzle exit, the liquid-gas interface is sharp and can be easily identified. However, when the jet is turbulent, the interface detection is less accurate. In that case, the interface position highly depends on the light threshold that is used for the measurement. In the numerical model used in this study, the interface is considered as diffused. The diffusion can be either numerical or due to turbulence. As the position of the interface is not calculated, it has to be reconstructed from results. As a consequence, a post-processing method has been implemented to detect the mean position of the interface using the same conditions of the experimental measurements, that is to say by analyzing instantaneous snapshots perpendicularly to the jet axis.

The instantaneous isosurface of $\alpha_l = 0.5$, which corresponds to the most probable position of the interface, is extracted from instantaneous fields from the simulation. At each position X, a slice of the isosurface is retrieved and the maximum radii of the jet found in 8 azimuthal planes are measured. An example of the method is presented in figure 13 where the radii of the jet in the 8 azimuthal sections are denoted as R_i, with $i = 1$ to 8.

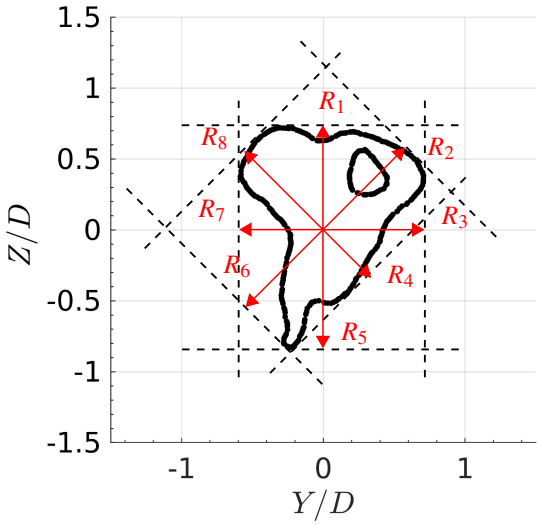

Fig. 13 Numerical interface detection method from a slice of the isosurface $\alpha_l = 0.5$.

The mean radius of the liquid jet obtained between $X = 0$ and $X/D = 40$ for the LES is plotted in figure 14. It is in good agreement with the experimental data. The mean radius is almost constant for $X/D < 15$ in the laminar part of the jet. For $X/D > 25$, it does not vary much and is a bit higher that the nozzle diameter. In the latter section, the liquid jet is developed and the liquid ligaments are slowly ejected from the liquid core resulting in a higher mean radius of the jet. There is a very good agreement between the experiment and the simulation in the transition region between $X/D = 15$ and $X/D = 20$.

The previous results are based on an experimental method for detecting the liquid-gas interface, necessary to compare experiment and simulation. Another method can be used directly from the LES mean field of liquid volume fraction, using an arbitrary criterion. For instance, the mean position of the maximum volume fraction gradient $max\left(\|\vec{\nabla}\alpha_l\|\right)$ is plotted in figure 15(a). A poor agreement with the experimental data is found in this case. The jet radius defined as the position where the volume fraction is equal to three specific values $\alpha_{l_{limit}}$ are represented in figures 15(b), 15(c) and 15(d). Using $\alpha_{l_{limit}} = 0.5$ in figure 15(b), the jet radius is in very good agreement with the experiment for $X/D < 10$ were the jet is laminar, but significantly differs for $X/D > 10$ where the jet is turbulent. For $\alpha_{l_{limit}} = 0.15$ in figure 15(c), the experimental and LES results are in very good concordance. Similar trends are obtained for $\alpha_{l_{limit}} = 0.1$ in figure 15(d).

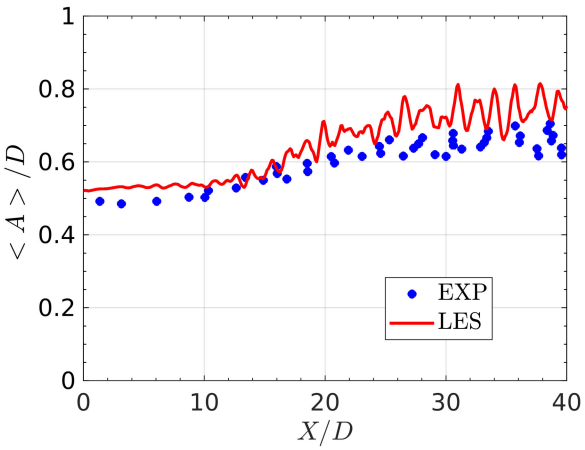

Fig. 14 Mean radius of the liquid jet.

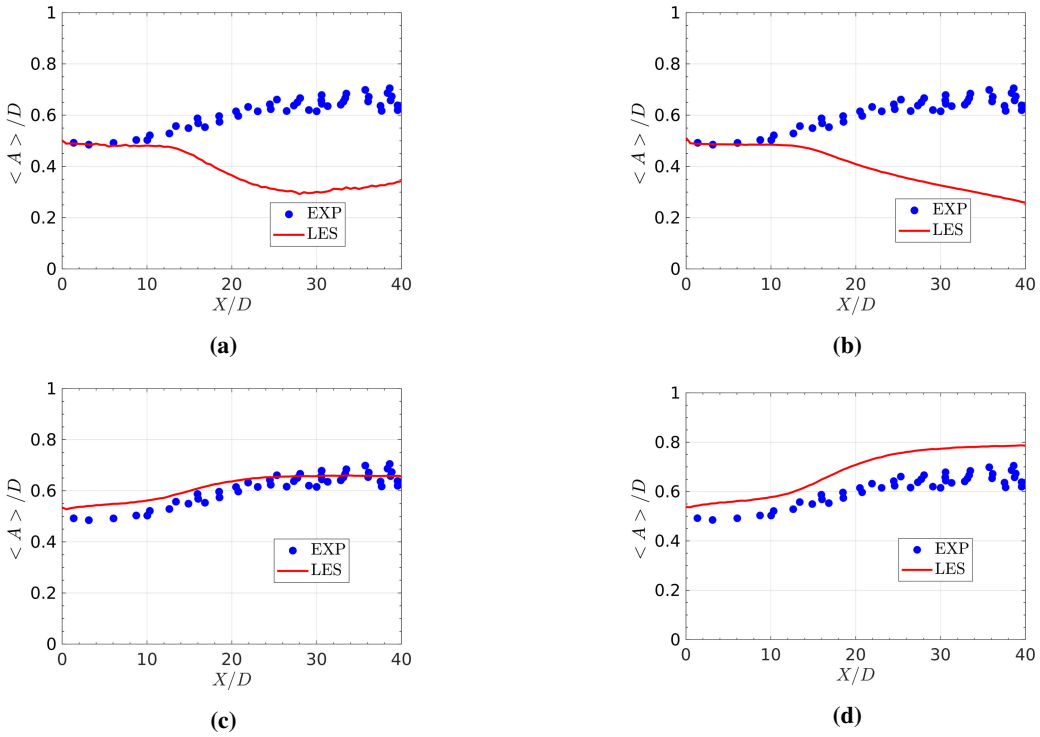

Fig. 15 Mean jet diameter based on different criteria for the LES : (a) $max\left(\|\vec{\nabla}\alpha_l\|\right)$, (b) $\alpha_{l_{limit}} = 0.5$, (c) $\alpha_{l_{limit}} = 0.15$, (d) $\alpha_{l_{limit}} = 0.1$.

To compare the radial profiles of volume liquid fraction at different axial positions, two non-dimensional numbers should be considered, namely the volume liquid fraction at the center of the jet α_{l_c} and the jet half-width related to the liquid volume fraction $r_{1/2} = r(\alpha_l = \alpha_{l_c}/2)$. The mean radial profiles of the liquid volume fraction are presented in figure 16 for $X/D = 210$ in the experiment and $X/D = 20$, 30 and 40 in the LES using the finer mesh. The LES profile at $X/D = 20$ is sharper than the experimental profile at $X/D = 210$, because the jet is not fully turbulent yet at $X/D = 20$. However, the LES profiles at $X/D = 30$ and $X/D = 40$ are similar to each other, and match the experimental profile. It can be deduced that beyond $X/D = 30$ the radial profile of volume liquid fraction does not change significantly and is self-similar.

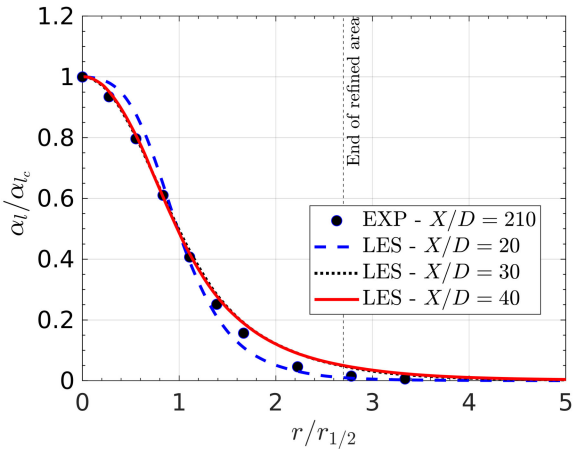

Fig. 16 Radial profiles of liquid volume fraction for the LES at $X/D = 20, 30, 40$ and for the experiment at $X/D = 210$.

3. Unstable mode identification

To identify the wave number of the interface instabilities, the fluctuations of the liquid-gas interface have been analyzed in Stevenin [25] based on the interface curvature defined as

$$C(s) = \frac{\frac{dx}{ds}\frac{d^2y}{ds^2} - \frac{dy}{ds}\frac{d^2x}{ds^2}}{\left(\left(\frac{dx}{ds}\right)^2 + \left(\frac{dy}{ds}\right)^2\right)^{3/2}} \tag{21}$$

where s is the curvilinear abscissa of the interface, and x and y are the coordinates of a point at the interface in the plane (X, Y). The variations of the curvature were measured from camera snapshots. As temporal signals are recorded at given locations in the simulation, the spatial spectra obtained in Stevenin [25] using curvature have been converted to temporal spectra at given locations using the convection velocity U_c. The Strouhal number is linked to the wave number k as :

$$St = \frac{DU_c}{2\pi U_{inj}} k \tag{22}$$

The convection velocity for the waves at the interface can be estimated, depending on the liquid and gas mean velocities and densities [47]:

$$U_c = \frac{\sqrt{\rho_l}U_l + \sqrt{\rho_g}U_g}{\sqrt{\rho_l} + \sqrt{\rho_g}} = 23.55\,\mathrm{m\,s^{-1}} \tag{23}$$

The Strouhal number of the peak components measured in Stevenin [25] are equal to $St = 2.4$ at $X/D = 13$ and $St = 1.2$ at $X/D = 25$.

The power spectral density of axial velocity computed from the LES data at $X/D = 0$, 10, 20 and 30 and at $r/D = 0.5$ are plotted in figure 17(a). At $X/D = 10$, a hump is clearly found around $St = 1.5$, whereas it is not the case at $X/D = 20$ and $X/D = 30$. The instability waves around $St = 1.5$ may be responsible for the jet transition. This value is comparable with the peak component found at $St = 2.4$ at $X/D = 13$ in the experiments. It should be noticed that the velocity difference between the gas and the liquid is higher in the experiment than in the simulation, due to the gas co-flow of $2\,\mathrm{m\,s^{-1}}$ in the LES. According to the work of Mayer and Branam [48], an increase in the velocity difference leads to an increase in the wave number of the interface instabilities. This could explain that the Strouhal number of maximum instabilities is a bit lower in the simulation than in the experiment. The power spectral densities obtained at $X/D = 10$ and $r/D = 0.5$ for grid sizes $\delta_{grid}/D = 0.0229$ and $\delta_{grid}/D = 0.0183$ are represented in figure 17(b). A finer mesh leads to the computation of more components in high frequencies, and a stronger hump. An increase in the grid size of 25 % leads to a decrease of the Strouhal number of the instability wave from $St = 1.5$ to $St = 1$.

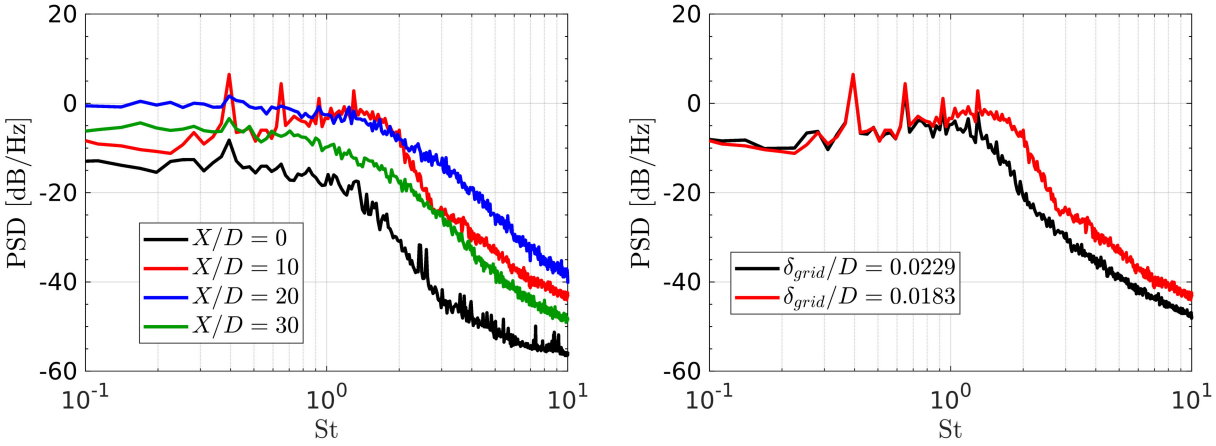

(a) **(b)**

Fig. 17 Power spectral density of U_x at $r/D = 0.5$: (a) for $\delta_{grid}/D = 0.0183$, (b) at $X/D = 10$, for $\delta_{grid}/D = 0.0229$ and $\delta_{grid}/D = 0.0183$.

C. Atomization of the liquid jet

The results of the simulation using both the dense and dispersed phase solvers are presented in this section. The coupling strategy detailed in section III.B is followed, but the diameter of the atomized droplets is unknown. A theoretical method based on the work of Marmottant and Villermaux [15] is applied to evaluate this diameter, using the wave number of the interface instabilities found in section IV.B.3.

1. Estimation of the droplet diameter

The instability waves which develop at the interface are amplified, and are subject to an azimuthal Rayleigh-Taylor (RT) instability [15]. In the study of Marmottant and Villermaux [15], this RT instability is linked to the initial interface wave. The RT wavelength depends on the interface instability wavelength λ_i as

$$\lambda_{RT} \simeq 2,45\lambda_i We_{\lambda_i}^{-1/3} \tag{24}$$

where $We_{\lambda_i} = \rho_g \parallel U_l - U_g \parallel \lambda_i/\sigma$ is the Weber number related to the interface instability.

The RT instability leads to the formation of ligaments whose diameter, for a sphere of equivalent volume, is experimentally found to be $D_l = 0.23\lambda_{RT}$. These ligaments break up to eject droplets with a diameter equal to $D_d \simeq 0,4D_l = 0,092\lambda_{RT}$. Given the instability wave emerging at $St = 1.5$ in the simulation, it is found that $We_{\lambda_i} = 23.3$, yielding $\lambda_{RT} \simeq \lambda_i$. The droplet diameter is then $D_d \simeq 0.092\lambda_i = 260\,\mu$m.

2. Simulation results with atomization

Simulations with atomization are carried out with the coarser mesh to evaluate the model at a reduced cost. The isosurfaces of the liquid volume fraction of the dense phase $\alpha_l = 0.15$ and of liquid volume fraction of the dispersed phase $\alpha_d = 0.005$ are presented in figure 18. Droplets are mostly present between $X/D \simeq 20$ and $X/D = 40$, where the jet is turbulent. The mean liquid volume fraction of droplets is shown in figure 19. For $X/D < 20$, where the jet is laminar, droplets can be found at the liquid-gas interface at $r/D \simeq 0.5$. Where the jet is turbulent, for $X/D > 20$, there is a significant amount of droplets on the center axis, whereas they are more diluted for $r/D > 0.5$.

The radial profiles of the liquid volume fraction of droplets at X/D =10, 20, 30 and 40 displayed in figure 20 give more quantitative results about the droplet locations. The maximum liquid volume fraction does not exceed 0.003 for $X/D < 20$, whereas it is significantly higher for $X/D = 30$ and $X/D = 40$. There is a local maximum at $r/D = 1.8$ for $X/D = 30$ and $r/D = 2$ for $X/D = 40$, in the liquid-gas turbulent mixing layer zone. The maximum values for $X/D = 30$ and $X/D = 40$ are located on the center axis, where the flow is not turbulent.

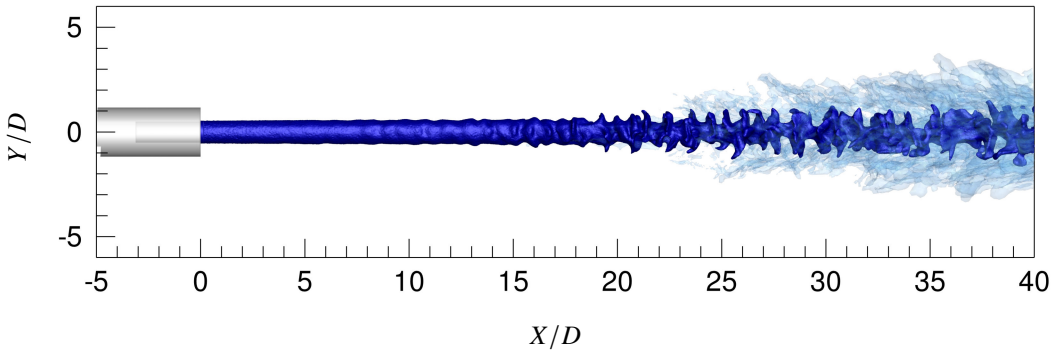

Fig. 18 Isosurfaces of $\alpha_l = 0.15$ in dark blue and $\alpha_d = 0.005$ in light blue.

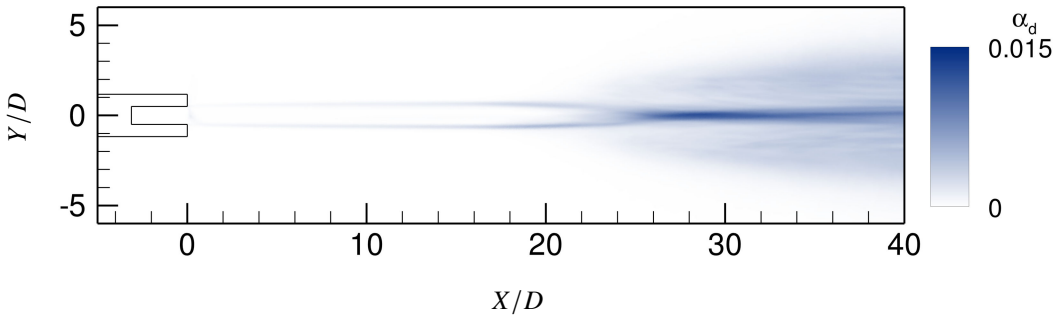

Fig. 19 Mean value of α_d in the (X, Y) plane.

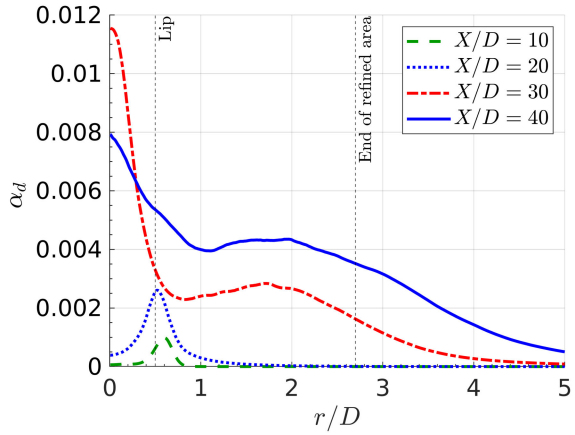

Fig. 20 Mean radial profiles of α_d.

To determine where the droplets are generated in the flow, the mean values of the atomization rate q_a are shown in figure 21. Droplets are mostly formed in the turbulent region which has been identified in section IV.B.1 between $X/D = 20$ and $X/D = 35$ in the shear layer, and the atomization rate is zero at the center axis. Therefore, the maximum concentration of droplets at the center line for $X/D > 20$ can be only explained by the droplet displacement from the lip line where they are created toward the jet axis.

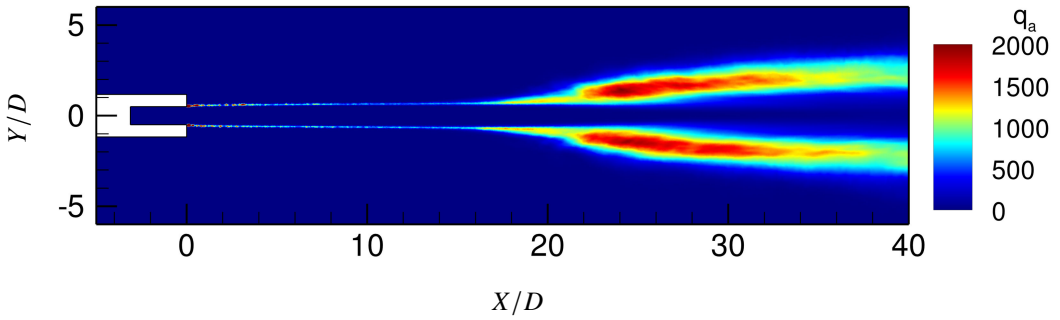

Fig. 21 Mean values of the atomization rate q_a [kg s^{-1} m^{-3}].

The mean values of droplet velocity U_{d_Y} in Y direction obtained in the turbulent region around $X/D = 20$ for $Y > 0$ are given in figure 22. In that region where most of the droplets are generated, they are negative, confirming that the droplets shift toward the center line once they are formed.

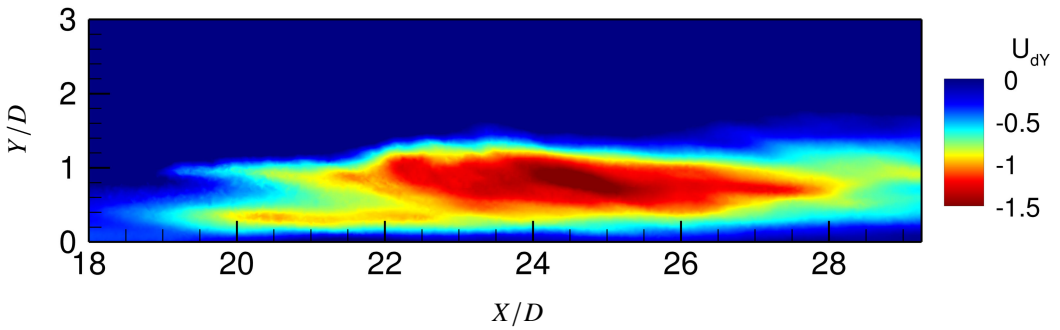

Fig. 22 Mean values of the droplet velocity U_{d_Y} in Y direction in the plane (X, Y) [m s^{-1}].

In the experiments [25, 26], data about droplet characteristics such as size, velocity and concentration are available only downstream of $X = 780D$. As it would be too costly to simulate the jet down to that distance, it is not possible to directly compare simulation results of the atomization with the measurements. However, general trends can be raised from the simulation results. It has been shown in Stevenin et al. [26] that, at $X/D = 780$, the Sauter mean diameter of the droplets, which is the ratio between the total volume of the particles and their total area, is about 1.5 mm on the center line, and decreases with the radial position to reach 1 mm at $r = 13.5D$. Thus, droplets at the center are sufficiently large to be directly calculated by the dense phase solver. The smallest droplets are located around the dense phase and must be calculated by the dispersed phase solver. Further investigations of this atomization model will be carried out to take into account the droplet re-absorption into the dense phase, that may contribute to the presence of large liquid ligaments at the center line.

V. Conclusion

In the present study, the LES of a water liquid jet exhausting into quiescent air has been carried out. The objective was to validate the calculation of the jet transition and the droplet generation based on an experiment from the literature. The analysis of the dense phase regime shows that the jet transitions when a turbulent inflow condition is settled with the synthetic-eddy method. This transition has been characterized by the investigation of the mean jet radius where a very good agreement is found between the simulation and the experiment. A clear hump in the power spectral density of axial velocity at $X/D = 10$ and $r/D = 0.5$ is obtained for a Strouhal number around 1.5 and may be responsible for the jet transition. The value of the instability wave frequency is of the same order of magnitude of the one found in the experiment at $St = 2.4$.

The instability analysis has then been used to determine the diameter of the atomized droplets in the model. The simulation of the jet with both the dense and dispersed phase solvers shows that droplets are mostly generated in the

turbulent regions of the flow, confirming that the atomization rate is well driven by the frequency f_a defined in the model. Moreover, the velocity of the droplets generated around $X/D = 25$ is slightly oriented toward the center line. This leads to an accumulation of droplets around the center. In future work, the re-absorption of particles into the dense phase will be considered, and could lower the droplet concentration on the jet axis.

The validation of the method proposed in this paper against experimental data from the literature will permit to address the case of the water nozzles used on the MARTEL test bench. A first analysis of the dense phase instabilities with the MARTEL injectors will give a characteristic wave number responsible for the jet transition, which will be used to estimate the droplet diameter. However, the water exhausting from the MARTEL nozzles is a flat liquid sheet, which thickness could have an influence on the ligament breakup mechanism.

Acknowledgments

This study is supported by the French space agency CNES and ONERA's scientific direction. Special acknowledgments are addressed to Hadrien Lambaré, research scientist at CNES and technical referee regarding the acoustic environment of rocket launchers, who helps connecting this project to the purpose of industrial rocket launchers.

References

[1] Bailly, C., and Bogey, C., "Propulsion system noise: jet," *Encyclopedia of Aerospace Engineering*, 2010. https://doi.org/10.1002/9780470686652.eae335.

[2] Tam, C. K. W., and Golebiowski, M., "On the two components of turbulent mixing noise from supersonic jets," *2nd AIAA/CEAS Aeroacoustics Conference*, 1996. https://doi.org/10.2514/6.1996-1716.

[3] McLaughlin, D. K., Morrison, G. L., and Troutt, T. R., "Experiments on the instability waves in a supersonic jet and their acoustic radiation," *Journal of Fluid Mechanics*, Vol. 69, No. 1, 1975, pp. 73–95. https://doi.org/doi:10.1017/S0022112075001322.

[4] Tam, C. K. W., and Tanna, H. K., "Shock associated noise of supersonic jets from convergent-divergent nozzles," *Journal of Sound and Vibration*, Vol. 81, No. 3, 1982, pp. 337–358. https://doi.org/10.1016/0022-460X(82)90244-9.

[5] Seiner, J. M., and Yu, J. C., "Acoustic near field properties associated with broadband shock noise," *AIAA Journal*, Vol. 22, No. 9, 1984, pp. 1207–1215. https://doi.org/10.2514/3.8762.

[6] Raman, G., "Advances in understanding supersonic jet screech: review and perspective," *Progress in Aerospace Sciences*, Vol. 34, No. 1,2, 1998, pp. 45–106. https://doi.org/10.1016/S0376-0421(98)00002-5.

[7] Zoppellari, E., "Évaluation expérimentale de la méthode de réduction du bruit des jets supersoniques chauds par injection d'eau," Ph.D. thesis, Ecole centrale de Lyon, 1997.

[8] Norum, T. D., "Reductions in multi-component jet noise by water injection," *10th AIAA/CEAS Aeroacoustics Conference*, 2004. https://doi.org/10.2514/6.2004-2976.

[9] Ignatus, J. K., Sankaran, S., Kumar, R. A., and Satyanarayana, T. N. V., "Suppression of jet noise by staged water injection during launch vehicle lift-off," *International Journal of Aeroacoustics*, Vol. 7, No. 3,4, 2008, pp. 223–242. https://doi.org/10.1260/1475-472X.7.3.223.

[10] Matas, J.-P., Marty, S., and Cartellier, A. H., "Experimental and analytical study of the shear instability of a gas-liquid mixing layer," *Physics of Fluids*, Vol. 23, No. 9, 2011, p. 094112. https://doi.org/10.1063/1.3642640.

[11] Lawrence, G. A., Browand, F. K., and Redekopp, L. G., "The stability of a sheared density interface," *Physics of Fluids A: Fluid Dynamics*, Vol. 3, No. 10, 1991, pp. 2360–2370. https://doi.org/10.1063/1.858175.

[12] Hoyt, J. W., and Taylor, J. J., "Waves on water jets," *Journal of Fluid Mechanics*, Vol. 83, No. 1, 1977, p. 119–127. https://doi.org/10.1017/S0022112077001074.

[13] Carpenter, J. R., Balmforth, N. J., and Lawrence, G. A., "Identifying unstable modes in stratified shear layers," *Physics of Fluids*, Vol. 22, No. 5, 2010, p. 054104. https://doi.org/10.1063/1.3379845.

[14] Varga, C. M., Lasheras, J. C., and Hopfinger, E. J., "Initial breakup of a small-diameter liquid jet by a high-speed gas stream," *Journal of Fluid Mechanics*, Vol. 497, 2003, pp. 405–434. https://doi.org/10.1017/S0022112003006724.

[15] Marmottant, P., and Villermaux, E., "On spray formation," *Journal of Fluid Mechanics*, Vol. 498, 2004, pp. 73–11. https://doi.org/10.1017/S0022112003006529.

[16] Lebas, R., Menard, T., Beau, P. A., Berlemont, A., and Demoulin, F. X., "Numerical simulation of primary break-up and atomization: DNS and modelling study," *International Journal of Multiphase Flow*, Vol. 35, No. 3, 2009, pp. 247–260. https://doi.org/10.1016/j.ijmultiphaseflow.2008.11.005.

[17] Tanguy, S., "Développement d'une méthode de suivi d'interface. Applications aux écoulements diphasiques," Ph.D. thesis, Université de Rouen, 2004.

[18] Chesnel, J., "Simulation aux grandes échelles de l'atomisation, application à l'injection automobile," Ph.D. thesis, Université de Rouen, 2010.

[19] Trontin, P., "Développement d'une approche de type LES pour la simulation d'écoulements diphasiques avec interface. Application à l'atomisation primaire," Ph.D. thesis, Institut supérieur de l'aéronautique et de l'espace, 2009.

[20] Marchesse, Y., "Étude expérimentale de la contribution des sources d'origine thermique à l'émission acoustique des jets supersoniques," Ph.D. thesis, Université de Poitiers, 2001.

[21] Fukuda, K., Tsutsumi, S., Shimizu, T., and Takaki, R., "Examination of sound suppression by water injection at lift-off of launch vehicles," *17th AIAA/CEAS Aeroacoustics Conference*, 2011. https://doi.org/10.2514/6.2011-2814.

[22] Capecelatro, J., and Buchta, D. A., "Direct numerical simulation of noise suppression by water injection in high-speed flows," *55th AIAA Sciences Meeting*, 2017. https://doi.org/10.2514/6.2017-1700.

[23] Salehian, S., and Mankbadi, R. R., "Simulations of rocket launch noise suppression with water injection from impingement pad," *International Journal of Aeroacoustics*, Vol. 19, No. 3-5, 2020, pp. 207–239. https://doi.org/10.1177/1475472X20930653.

[24] Gely, D., Valière, J.-C., Lambaré, H., and Foulon, H., "Overview of aeroacoustic research activities in MARTEL facility applied to jet noise," *INTER-NOISE and NOISE-CON Congress and Conference Proceedings*, 2006, pp. 1282–1290.

[25] Stevenin, C., "Étude de l'atomisation d'un jet d'eau haute vitesse. Application à l'irrigation par aspersion et à la pulvérisation," Ph.D. thesis, Ecole Centrale Marseille, 2012.

[26] Stevenin, C., Vallet, A., Tomas, S., Amielh, M., and Anselmet, F., "Eulerian atomization modeling of a pressure-atomized spray for sprinkler irrigation," *International Journal of Heat and Fluid Flow*, Vol. 57, 2015, pp. 142–149. https://doi.org/10.1016/j.ijheatfluidflow.2015.11.010.

[27] Refloch, A., Courbet, B., Murrone, A., Villedieu, P., and Laurent, C. e. a., "CEDRE Software," *AerospaceLab*, 2011.

[28] Magnaudet, J., Rivero, M., and Fabre, J., "Accelerated flows past a rigid sphere or a spherical bubble. Part 1. Steady straining flow," *Journal of Fluid Mechanics*, Vol. 284, 1995, pp. 97–135. https://doi.org/10.1017/S0022112095000280.

[29] Tryggvason, G., Bunner, B., Esmaeeli, A., Juric, D., Al-Rawahi, N., Tauber, W., Han, J., Nas, S., and Jan, Y.-J., "A front-tracking method for the computations of multiphase flow," *Journal of Computational Physics*, Vol. 169, No. 2, 2001, pp. 708–759. https://doi.org/10.1006/jcph.2001.6726.

[30] Sethian, J. A., "A fast marching level set method for monotonically advancing fronts," *Proceedings of the National Academy of Sciences*, Vol. 93, No. 4, 1996, pp. 1591–1595. https://doi.org/10.1073/pnas.93.4.1591.

[31] Enright, D., Fedkiw, R., Ferziger, J., and Mitchell, I., "A hybrid particle Level Set method for improved interface capturing," *Journal of Computational Physics*, Vol. 183, No. 1, 2002, pp. 83–116. https://doi.org/10.1006/jcph.2002.7166.

[32] Rutard, N., Dorey, L.-H., Le Touze, C., and Ducruix, S., "Large-eddy simulation of an air-assisted liquid jet under a high-frequency transverse acoustic forcing," *International Journal of Multiphase Flow*, Vol. 122, 2019. https://doi.org/10.1016/j.ijmultiphaseflow.2019.103144.

[33] Gaillard, P., Le Touze, C., Matuszewski, L., and Murrone, A., "Numerical simulation of cryogenic injection in rocket engine combustion chambers," *Journal Aerospace Lab*, 2016, pp. 1–11.

[34] Jarrin, N., Benhamadouche, S., Laurence, D., and Prosser, R., "A Synthetic-Eddy-Method for generating inflow conditions for large-eddy simulations," *International Journal of Heat and Fluid Flow*, Vol. 27, No. 4, 2006, pp. 585–593. https://doi.org/10.1016/j.ijheatfluidflow.2006.02.006.

[35] Jarrin, N., Prosser, R., Uribe, J.-C., Benhamadouche, S., and Laurence, D., "Reconstruction of turbulent fluctuations for hybrid RANS/LES simulations using a Synthetic-Eddy Method," *International Journal of Heat and Fluid Flow*, Vol. 30, No. 3, 2009, pp. 435–442. https://doi.org/10.1016/j.ijheatfluidflow.2009.02.016.

[36] Jarrin, N., "Synthetic inflow boundary conditions for the numerical simulation of turbulence," Ph.D. thesis, University of Manchester, 2008.

[37] Reitz, R. D., *Atomization and other breakup regimes of a liquid jet*, University Microfilms International, 1978.

[38] Lasheras, J. C., and Hopfinger, E. J., "Liquid jet instability and atomization in a coaxial gas stream," *Annual Review of Fluid Mechanics*, Vol. 32, No. 1, 2000, pp. 275–308. https://doi.org/10.1146/annurev.fluid.32.1.275.

[39] Stahl, M., Gnirb, M., Damaschke, N., and Tropea, C., "Laser doppler measurements of nozzle flow and optical characterisation of the generated spray," *20th ILASS - Europe Meeting*, 2005, pp. 337–342.

[40] Le Touze, C., "Couplage entre modèles diphasiques à "phases séparées" et à "phase dispersée" pour la simulation de l'atomisation primaire en combustion cryotechnique," Ph.D. thesis, Université Nice Sophia Antipolis, 2015.

[41] Smagorinsky, J., "General circulation experiments with the primitive equations. I. The basic experiment," *Monthly Weather Review*, Vol. 91, No. 3, 1963, pp. 99–164. https://doi.org/10.1175/1520-0493(1963)091<0099:GCEWTP>2.3.CO;2.

[42] Toro, E. F., Spruce, M., and Speares, W., "Restoration of the contact surface in the HLL-Riemann solver," *Shok Waves*, Vol. 4, No. 1, 1994, pp. 25–34. https://doi.org/https://doi.org/10.1007/BF01414629.

[43] Le Touze, C., Murrone, A., and Guillard, H., "Multislope MUSCL method for general unstructured meshes," *Journal of Computational Physics*, Vol. 284, 2015, pp. 389–418. https://doi.org/https://doi.org/10.1016/j.jcp.2014.12.032.

[44] Williams, F. A., "Spray combustion and atomization," *The Physics of Fluids*, Vol. 1, No. 6, 1958, pp. 541–545. https://doi.org/10.1063/1.1724379.

[45] Schiller, L., and Naumann, Z., "A drag coefficient correlation," *Zeit. Ver. Deutsch. Ing.*, 1935, pp. 77–318.

[46] Wu, P.-K., Miranda, R. F., and Faeth, G. M., "Effects of initial flow conditions on primary breakup of nonturbulent and turbulent liquid jets," *32nd Aerospace Sciences Meeting and Exhibit*, 1994. https://doi.org/10.1615/AtomizSpr.v5.i2.40.

[47] Dimotakis, P. E., "Two-dimensional shear-layer entrainment," *AIAA Journal*, Vol. 24, No. 11, 1986, pp. 1791–1796. https://doi.org/10.2514/3.9525.

[48] Mayer, W. O. H., and Branam, R., "Atomization characteristics on the surface of a round liquid jet," *Experiments in Fluids*, Vol. 36, No. 4, 2004, pp. 528–539. https://doi.org/10.1007/s00348-003-0675-0.